

Figure 5 Filtering characteristic of the MRCR

size of the unit cell of the double-ring. In fact, the structure with a single negative permeability is much simpler than a double-negative LHM in designs and fabrications.

REFERENCES

1. N. Engheta and R.W. Ziolkowski, A positive future for double-negative metamaterials, *IEEE Trans Microwave Theory Tech* 53 (2005), 1535–1555.
2. R.A. Shelby, D.R. Smith, and S. Schultz, Experimental verification of negative index of refraction, *Science* 292 (2001), 77–79.
3. J.B. Pendry, A chiral route to negative refraction, *Science* 306 (2004), 1353–1355.
4. R.W. Ziolkowski and C.-Y. Cheng, Existence and design of transvacuum-speed metamaterials, *Phys Rev E* 68 (2003), 026612–026618.
5. K. Buell, H. Mosallaei, and K. Sarabandi, A substrate for small patch antennas providing tunable miniaturization factors, *IEEE Trans Microwave Theory Tech* 54 (2006), 135–145.
6. S. Lim, C. Caloz, and T. Itoh, A reflecto-directive system using a composite right/left-handed (crlh) leaky-wave antenna and heterodyne mixing, *IEEE Microwave Wireless Compon Lett* 14 (2004), 183.
7. S. Hrabar, J. Bartolic, and Z. Sipus, Waveguide miniaturization using uniaxial negative permeability metamaterial, *IEEE Trans Antenna Propagat* 53 (2005), 110–119.
8. R. Marques, J. Martel, F. Mesa, and F. Medina, Left-handed-media simulation and transmission of em waves in subwavelength split-ring-resonator-loaded metallic waveguides, *Phys Rev Lett* 89 (2002), 183901–183904.
9. J. Perruisseau-Carrier and A. K. Skrivervik, Composite right/left-handed transmission line metamaterial phase shifters (mps) in mmic technology, *IEEE Trans Microwave Theory Tech* 54 (2006), 1582.
10. M.A. Antoniades and G.V. Eleftheriades, Compact linear lead/lag metamaterial phase shifters for broadband applications, *IEEE Antenna Wireless Propagat Lett* 2 (2003), 103.
11. N. Engheta, An idea for thin subwavelength cavity resonators using metamaterials with negative permittivity and permeability, *IEEE Antenna Wireless Propagat Lett* 1 (2002), 10–13.
12. Y. Li, L. Ran, H. Chen, J. Huangfu, X. Zhang, K. Chen, T.M. Grzegorzcyk, and J.A. Kong, Experimental realization of a one-dimensional LHM-RHM resonator, *IEEE Trans Microwave Theory Tech* 53 (2005), 1521.
13. R. Marques, F. Medina, and R. Rafii-El-Idrissi, Role of bianisotropy in negative permeability and left-handed metamaterials, *Phys Rev B* 65 (2002), 144441–144446.
14. D.R. Smith, W.J. Padilla, D.C. Vier, S.C. Nemat-Nasser, and S. Schultz, Composite medium with simultaneously negative permeability and permittivity, *Phys Rev Lett* 84 (2000), 4184–4187.

© 2008 Wiley Periodicals, Inc.

ESTIMATION OF THE FIBER TEMPERATURE DURING AN ARC-DISCHARGE

Gaspar Rego,^{1,2} Luís M. N. B. F. Santos,³ and Bernd Schröder³

¹Escola Superior de Tecnologia e Gestão, Av. do Atlântico, 4900-348 Viana do Castelo, Portugal; Corresponding author: gmrego@fc.up.pt

²UOSE, INESC-Porto, Rua do Campo Alegre 687, 4169-007 Porto, Portugal

³Centro de Investigação em Química, Departamento de Química, FCUP, Rua do Campo Alegre 687, 4169-007 Porto, Portugal

Received 30 November 2007

ABSTRACT: The formation mechanisms and properties of arc-induced gratings are intrinsically related to the temperature attained by the fiber during arc exposure. In this work, we present further results on the estimation of the fiber temperature based on the use of electrically insulated thermocouples. Computer simulations show that under typical arc discharge conditions, the fiber reaches steady-state thermal equilibrium in less than half a second, having a peak temperature of about 1350°C.

© 2008 Wiley Periodicals, Inc. *Microwave Opt Technol Lett* 50:

2020–2025, 2008; Published online in Wiley InterScience (www.interscience.wiley.com). DOI 10.1002/mop.23555

Key words: temperature measurement; steady-state thermal equilibrium; time constant; thermally insulated thermocouples; electric arc discharge; arc-induced gratings; long-period gratings; fiber gratings

1. INTRODUCTION

In recent years, some effort has been applied in finding the formation mechanisms of arc-induced gratings [1–4]. In this context, the determination of the temperature reached by the fiber during the electric arc discharge is an essential parameter for the correct assessment of the influence of each potential mechanism. Recently, based on blackbody radiation, we estimated a value of $(1400 \pm 50)^\circ\text{C}$ for the fiber temperature [5]. In a previous work carried out using electrically insulated thermocouples [6], a value of $\sim 1320^\circ\text{C}$ was obtained for the temperature attained by an optical fiber during an arc discharge. In that approach, the basic requirements were as to guarantee that the arc discharge remained unperturbed and that the temperature sensor had dimensions comparable to those of an optical fiber. That was achieved by fabricating a thermocouple inside a silica capillary with an outer diameter similar to that of a standard optical fiber. In this way, the electrical isolation of the thermocouple is also guaranteed. Note, however, that since the thermocouple has a thermal conductivity different from that of silica glass, the temperature reached by an optical fiber during an arc discharge is necessarily different from that of this measuring system. Therefore, the following methodology was used. First, the temperature distribution in the thermocouple was measured and then the temperature profile for an optical fiber was estimated through a simplified heat transfer model simulated by a finite element method using a commercial partial differentiation solver. It should be stressed that the results obtained strongly depend on the temperature dependence of the physical parameters involved in the simulations. This technique comprises less intermediate steps and assumptions than the one based on blackbody radiation and, therefore, is more reliable. Recently, new data related to type S thermocouples appeared in the literature [7] allowing us to improve the previous result. In this work, we started with estimating the time required for a fiber to reach a steady-state thermal equilibrium. This knowledge is particularly important in situations where two or more mechanisms

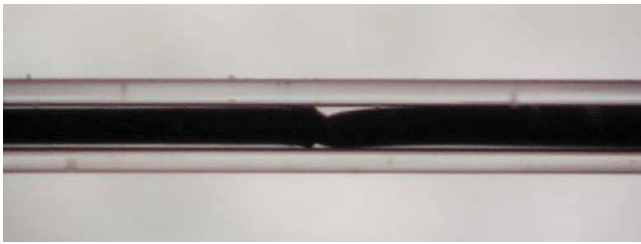


Figure 1 Pt/Pt-Rh thermocouple (wires with a diameter of 50 μm). [Color figure can be viewed in the online issue, which is available at www.interscience.wiley.com]

(having distinct time-dependent properties) may compete for the formation of the grating [4]. Thus by controlling the arc duration during the gratings fabrication, one can enhance the contribution of one of the mechanisms. Afterwards, based on the new equations for the temperature dependence of the thermal conductivity of the platinum-rhodium alloys, we re-evaluated the results obtained in Ref. 6. Also, we present for the first time details on the computer simulations and the temperature dependence of all physical parameters used in the calculations. This way, we clarify the previous methodology and allow others to pursue the improvement of this technique.

2. EXPERIMENTAL RESULTS

Three electrically insulated thermocouples, having different diameters (in micrometers), were produced as described in Ref. 6. A photograph of the 50/50 thermocouple fabricated by applying arc discharges is shown in Figure 1. Following the thermocouple assembly, arc discharges with an electric current of 9 mA and 3 s duration were applied to the thermocouple junction. The voltage in the thermocouples was measured using an Agilent 34401A multimeter, controlled by a LabView program. Afterwards, the voltage values were converted to temperature using the reference function for type S thermocouples based on the ITS-90 [8].

2.1. Estimation of the Thermal Unsteady-State Duration

Considering the fiber submitted to an arc-discharge as a simple single body-model, the rate of change of temperature can be assumed to be described by Newton's law of heat transfer,

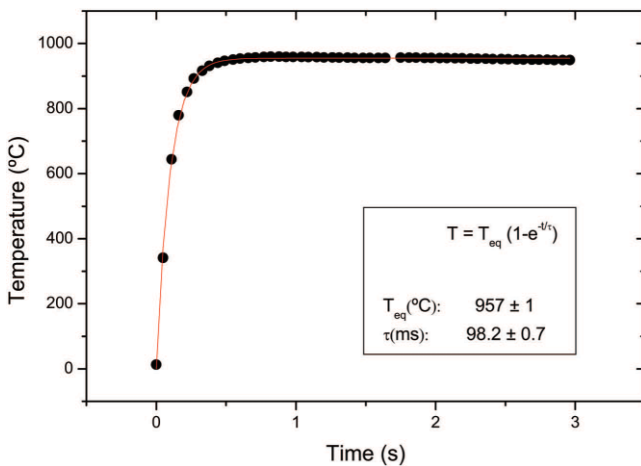


Figure 2 Time constant for the 50 μm -thermocouple obtained by fitting the temperature evolution at the thermocouple junction as depicted in Fig. 1. [Color figure can be viewed in the online issue, which is available at www.interscience.wiley.com]

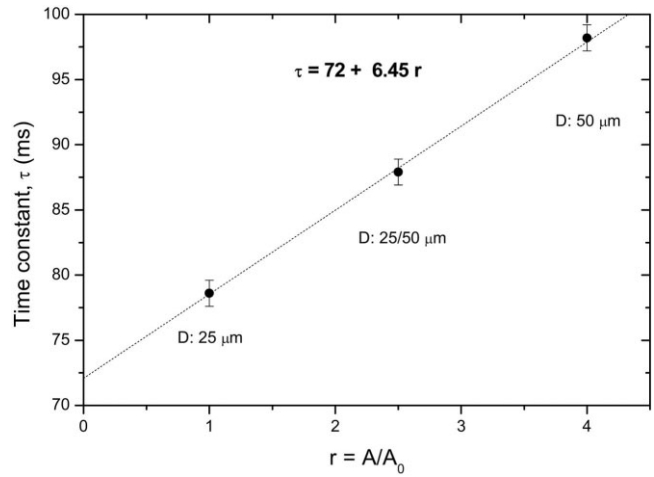


Figure 3 Time constants for the three thermocouples

$$dT/dt = Lm(T_\infty - T) \quad (1)$$

where T is the temperature; t is the time; T_∞ is the convergence temperature that can be derived from the condition of a pseudo steady-state thermal equilibrium, in which the heat exchange balance is reached, and where $dT/dt = 0$; Lm is the thermal leakage modulus (overall heat-transfer coefficient to the surroundings divided by the total effective heat capacity).

The analytical integration of Eq. (1) gives an exponential function that describes the temperature in the fiber submitted to an arc discharge, $T(t)$, as a function of the time, t , considering an initial point, (T_i, t_i) ,

$$T(t) = T_\infty - (T_\infty - T_i)\exp\{-Lm(t - t_i)\} \quad (2)$$

For practical reasons, Lm , is usually expressed in the form of a time constant,

$$\tau = Lm^{-1}$$

The time constant could be expressed and analyzed as a constant resulting from the ratio between the overall effective heat capacity and the heat-transfer coefficient.

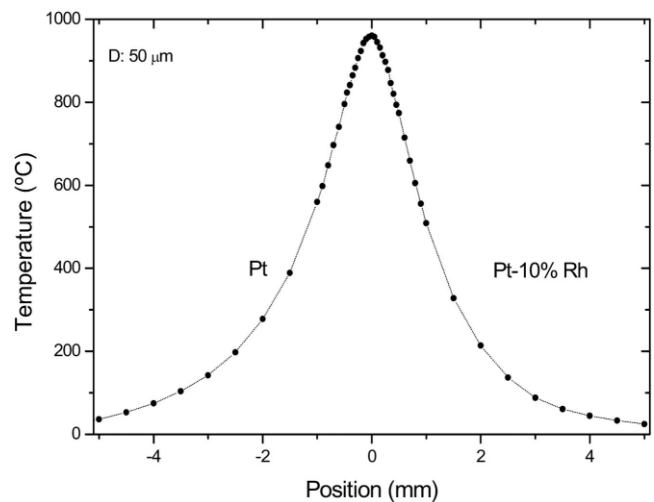


Figure 4 Temperature distribution in the 50 μm -type S thermocouple

TABLE 1 Temperature Dependence of the Physical Parameters Used in the Simulations (T in Kelvin)

Designation	Expression	Range
Thermal conductivity of air [10]	$k = 3.84 \times 10^{-3} + 7.66 \times 10^{-5}T - 1.54 \times 10^{-8}T^2$	
Convection heat transfer coefficient of air [10]	$h(56) = 310.197 + 2.392 \times 10^{-1}T - 1.906 \times 10^{-5}T^2$	$T > 1200$ K
idem (external surface) [10]	$h(125) = 55.910 + 3.249 \times 10^{-1}T - 1.164 \times 10^{-4}T^2$	$T < 1100$ K
Thermal conductivity of Pt [7]	$k = 77.8 + 2.15 \times 10^{-2}(T - 300)$	
Thermal conductivity of Pt/Rh [7]	$k = 43.5 + 4.3 \times 10^{-2}(T - 300)$	
Specific heat of Pt [9]	$C_p = 125.15 + 2.655 \times 10^{-2}T$ $\bar{C}_p = \frac{1.3 \times 10^5 + (T - 1173)[C_p(T) + 156.3]/2}{T - 293}$	$T > 1200$ K
Density of Pt	$\rho = \frac{21450}{1 + 3a}$ $a = 9.122 \times 10^{-4}(T - 293) + 7.467 \times 10^{-8}(T - 293)^2 + 4.258 \times 10^{-11}(T - 293)^3$ $\bar{\rho} = \frac{1.864 \times 10^7 + (T - 1173)[\rho(T) + 20892.4]/2}{T - 293}$	
Specific heat of SiO ₂ [9]	$C_p = \frac{T - 2 \times 10^5}{23.1992 + T} + 1.7 \times 10^{-3}(T + 8 \times 10^5)$ $\bar{C}_p = \frac{5.666 \times 10^5 + (T - 900)[C_p(T) + 1153]/2}{T - 300}$	
Density of SiO ₂ [11]	$\rho = \begin{cases} 2222.5 - 9.10 \times 10^{-3}T \\ 2426.0 - 1.57 \times 10^{-1}T \end{cases}$ $\bar{\rho} = \begin{cases} \frac{2.171 \times 10^6 + (T - 1273)[\rho(T) + 2210.9]/2}{T - 293} \\ \frac{2.392 \times 10^6 + (T - 1373)[\rho(T) + 2210]/2}{T - 293} \end{cases}$	$T \leq 1400$ K $T > 1400$ K $T \leq 1400$ K $T > 1400$ K
Thermal conductivity of SiO ₂ [9, 10]	$k = \begin{cases} -48.661 + 1.349 \times 10^{-1}T - 1.208 \times 10^{-4}T^2 + 3.75 \times 10^{-8}T^3 \\ 7.8 \times 10^{-1} - 5.4 \times 10^{-2}e^{\frac{T+379}{354}} + 1.65 \times 10^{-1}e^{\frac{T+379}{405}} \end{cases}$	$T \geq 1000$ K $T < 1000$ K
Emissivity of SiO ₂ [12]	$\varepsilon = 0.056 + 1.90e^{-\frac{T}{552}}$	$T > 900$ K

To estimate the time required for a fiber submitted to an arc-discharge to reach the steady-state thermal equilibrium, we proceeded as follows. First, the time constants for the three thermocouples were obtained by fitting the curves corresponding to the time dependence of the temperature at the thermocouple junction (see Fig. 2). Then, by extrapolation of the data for the case of having no thermocouple (zero diameter), the time constant for the silica capillary (external and internal diameters of 125 and 56 μm , respectively) was estimated to be 72 ± 2 ms (see Fig. 3). Afterwards, by taking the ratio of the cross sections for the fiber and the capillary, a value of 90 ms was obtained for the time constant of the optical fiber. Therefore, the fiber reaches steady-state thermal equilibrium (the time required to achieve 99% of the stationary temperature) in about 415 ms.

Recently [4], we demonstrated that, under certain conditions, it is possible to fabricate in a B/Ge co-doped fiber an arc-induced long-period grating (LPG) whose spectrum contains a dual set of resonances. These two sets of resonances are formed by distinct mechanisms (densification and microdeformation) and are caused by coupling to cladding modes of different symmetries. These formation mechanisms depend differently on time; initially the former dominates and afterwards is microdeformation that prevails due to a linear dependence on time [2]. Therefore, by adjusting the arc duration, the contribution of one of the mechanisms to the gratings formation can be increased.

2.2. Estimation of the Capillary Temperature

Arc discharges in steps of tenths to hundreds of micrometers were also applied on both sides of the thermocouple junction, covering a region of 10 mm. Figure 4 shows the temperature distribution in the 50 μm thermocouple. The peak temperature of the capillary was obtained assuming that as the energy dissipated through the wires approaches zero, the thermocouple temperature would approach the capillary temperature without thermocouple. The energy dissipated through the wires, per unit of time, P_d , was calculated using the standard heat transfer expression for conduction

$$P_d = -k_{\text{Pt}} \left(\frac{\pi}{4} D_T^2 \right) \left(\frac{\Delta T}{L} \right)_{\text{Pt}}$$

in which k , D_T and $\Delta T/L$ represent, respectively, the thermal conductivity of the thermocouple wire, its diameter and the temperature gradients in the vicinity of the thermocouple junction. The temperature dependence of the thermal conductivity for platinum was taken from the literature [9], whereas for the alloy it was estimated based on data from a recent article in which several platinum alloys were examined at high temperatures [7]. Although at room temperature, the thermal conductivity of platinum is almost twice that for the alloy, at high temperatures both have similar values due to the higher temperature coefficient of the thermal conductivity for the platinum alloy. In fact, it was exper-

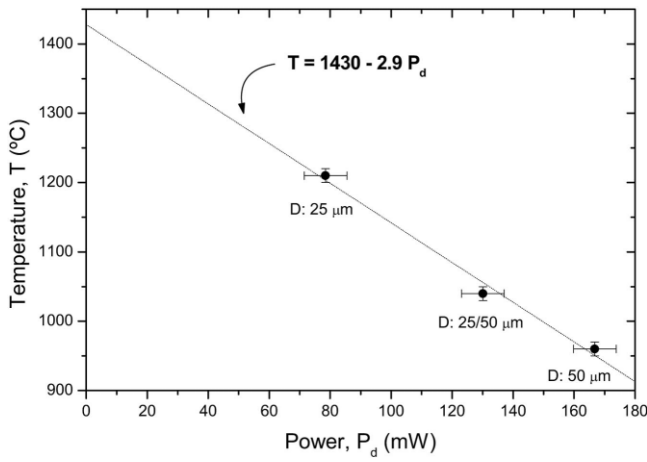


Figure 5 Peak temperature versus power dissipated through the thermocouples

imentally observed from data concerning the power dissipation in thermocouples composed of wires with different diameters, that the difference between the thermal conductivities of platinum and the alloy decreases from about 45% at room temperature to 15% at 1000°C (see Table 1). The result of this analysis is shown in Figure 5, where the peak temperature measured by three thermocouples with different diameters is plotted as a function of the power dissipated in the thermocouples. The error bars referring to the x -axis account for the uncertainty of the diameter of the thermocouples ($\pm 1 \mu\text{m}$) and on the thermal conductivity of the alloy (10%), whereas the error bars referring to the y -axis account for the uncertainty in the thermocouple positioning between the electrodes which, in turn, affects the temperature measurement ($\pm 10^\circ\text{C}$). The linear fitting applied to the experimental data points towards a capillary temperature of $\sim 1430^\circ\text{C}$ with an overall uncertainty of $\pm 50^\circ\text{C}$.

2.3. Estimation of the Fiber Temperature

To determine the temperature profile in the fiber, several steps are required. First, the experimental temperature profiles in the thermocouples (see Fig. 4) are fitted to the simulation results by tuning the thermal power delivered by the arc, the dimensions of the point source used and the separation between the point source and the silica capillary. Second, the thermocouples are removed from the

previous system and for the same power, the temperature profile in the capillary is derived. This allows a comparison between the peak temperature of the capillary and the value estimated graphically (see Fig. 5). Finally, a similar calculation is performed for the case of having an optical fiber instead of the capillary. Note that for each set of thermocouples, independent simulations were realized using a simplified heat transfer model of the assembly based on a finite element analysis. Radial heat transfer was simulated by a finite element method using a commercial partial differentiation solver (Flex PDE 2.13 from PDE Solutions Inc. [13]), assuming a two-dimensional steady-state conduction model, which holds for the period after thermal stationary equilibrium is reached. The boundary conditions applied to the dash box shown in Figure 6 are as follows: heat is transferred to the system through a narrow arc discharge, the internal radiative heat transfer within the silica capillary is neglected but radiative heat transfer is considered at the capillary surface, along with a convection contribution; by symmetry there is no heat transfer along the axis of the thermocouple and the boundary is at room temperature (25°C). Figure 6 summarizes the types of heat transfer involved in the simulations. Table 1 gives the expressions for the temperature dependence of the physical parameters used in the simulations. The dimensions of the point source and its distance to the silica capillary were set equal to 5 and $412.5 \mu\text{m}$ (electrodes' gap equal to $950 \mu\text{m}$), respectively. The results obtained from simulations for the $50 \mu\text{m}$ thermocouple are shown in Figures 7–9, corresponding to the various steps taken to obtain the temperature profile for the fiber. Figure 7 shows the temperature distribution of the whole system consisting of the thermocouple and capillary arrangement. The temperature profile of the silica capillary with the thermocouple inserted is shown in Figure 8. A value of 1045°C was obtained for the peak temperature, which is about 85°C above the value obtained for the temperature in the thermocouple junction (see Figs. 2 and 4). The estimated temperature profiles, obtained from computer simulations, in the capillary and in a fiber are shown in Figure 9. The correspondent capillary peak temperature is of about 1445°C , in good agreement with the value obtained from Figure 5. The peak value of the fiber temperature of $\sim 1350^\circ\text{C}$ is also in good agreement with the value obtained through the blackbody radiation method [5].

A final remark to the fact that in the computer simulations it was assumed a cylindrical symmetry, but we have demonstrated recently that the arc discharge is indeed directional what causes a temperature gradient in the fiber [2]. Therefore, depending on the

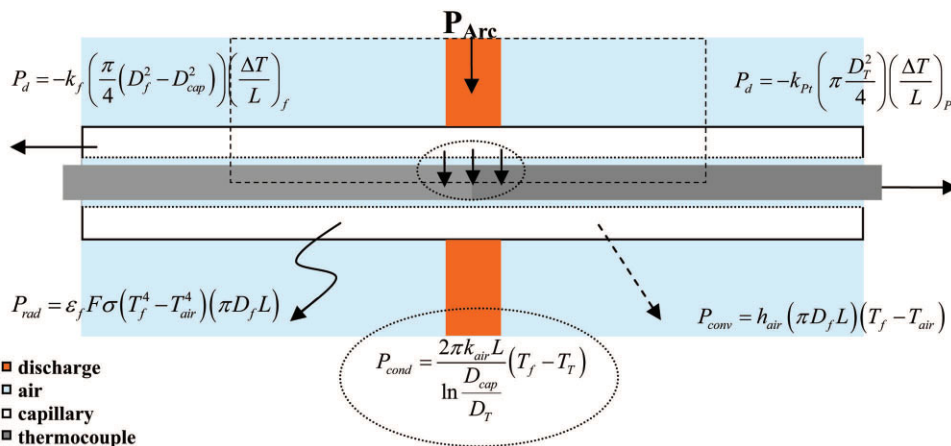


Figure 6 Heat transfer equations for the system consisting of a silica capillary, with a thermocouple inside, submitted to an arc discharge through air. [Color figure can be viewed in the online issue, which is available at www.interscience.wiley.com]

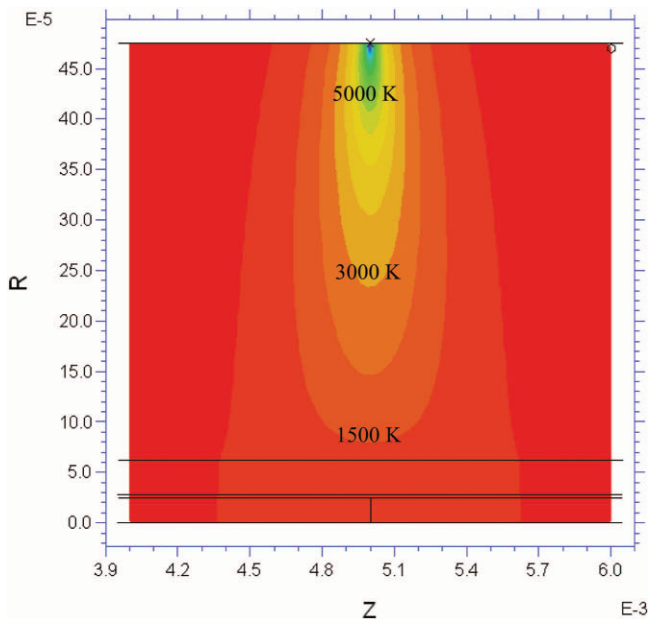


Figure 7 Temperature distribution (in Kelvin) in the system consisting of thermocouple and capillary: R is the radius from the thermocouple axis up to the point source ($475 \mu\text{m}$) and Z is the distance from the thermocouple junction ($5 \pm 1 \text{ mm}$). [Color figure can be viewed in the online issue, which is available at www.interscience.wiley.com]

position of the fiber relative to the line joining the two electrodes, a temperature difference through the fiber cross-section ranging from 20 up to 80°C can be achieved.

3. CONCLUSIONS

We present details of the computer simulations associated to the technique, based on electrically insulated thermocouples, for the

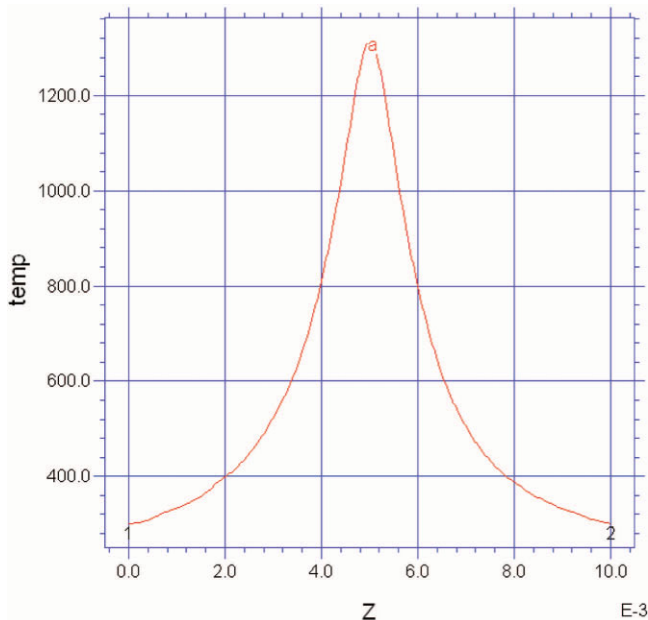


Figure 8 Simulation result corresponding to the temperature profile (in Kelvin) of the silica capillary with the $50 \mu\text{m}$ thermocouple inserted ($T_{\text{peak}} = 1045^\circ\text{C}$). [Color figure can be viewed in the online issue, which is available at www.interscience.wiley.com]

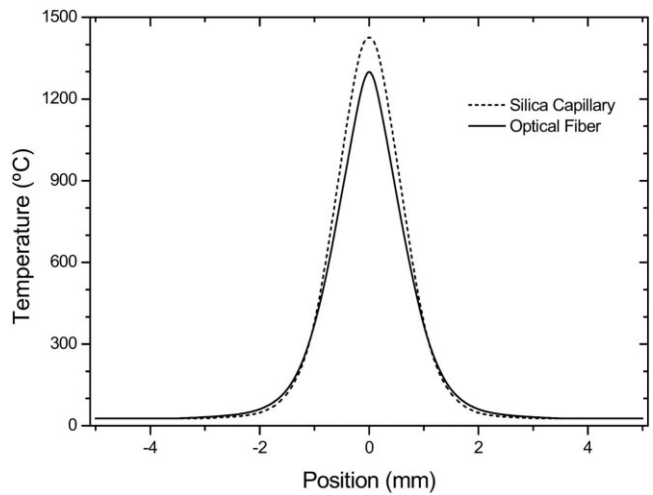


Figure 9 Temperature profiles in the capillary and in the fiber computed by finite element analysis

measurement of the temperature of an optical fiber whilst being heated through electric arc discharges. By following the time evolution of the temperature in the thermocouples, it was estimated that a fiber achieves steady-state thermal equilibrium in about 0.4 s . For a current of 9 mA , a capillary temperature of $(1430 \pm 50)^\circ\text{C}$ was obtained by extrapolation of the experimental data for near-zero diameter thermocouples. The temperature profiles in the capillary and in the optical fiber were determined by solving the classical heat transfer equations making use of the data obtained for the thermocouples with different diameters. The respective peak temperatures calculated for the fiber (capillary) was of about 1350°C (1445°C). The fiber temperature values agree well with those obtained using other techniques [5]. This method allows the measurement of an important parameter, the fiber temperature under electrical arc discharges that concerns not only the control of the LPGs fabrication process, but also the mechanisms responsible for their formation. Furthermore, it is expected that these electrically insulated temperature microsensors can also play an important role in the adjustment of the arc parameters of fusion splicing machines [14].

REFERENCES

1. G. Rego, O. Ivanov, and P.V.S. Marques, Demonstration of coupling to symmetric and antisymmetric cladding modes in arc-induced long-period fiber gratings, *Opt Express* 14 (2006), 9594–9599.
2. O. Ivanov and G. Rego, Origin of coupling to antisymmetric modes in arc-induced long-period fiber gratings, *Opt Express* 15 (2007), 13936–13941.
3. F. Durr, G. Rego, P.V.S. Marques, S.L. Semjonov, E. Dianov, H.G. Limberger, and R.P. Salathé, Tomographic stress profiling of arc-induced long period fiber gratings, *J Lightwave Technol* 23 (2005), 3947–3953.
4. G. Rego and O. Ivanov, Two types of resonances in long-period gratings induced by arc discharges in B/Ge co-doped fibers, *Opt Lett* 32 (2007), 2984–2986.
5. G. Rego, P.V.S. Marques, J.L. Santos, and H.M. Salgado, Estimation of the fibre temperature during the inscription of arc-induced gratings, *Opt Commun* 259 (2006), 620–625.
6. G. Rego, L.M.N.B.F. Santos, B. Schröder, P.V.S. Marques, J.L. Santos, and H.M. Salgado, In situ temperature measurement of an optical fiber submitted to electric arc discharges, *IEEE Photon Technol Lett* 16 (2004), 2111–2114.
7. Y. Terada, Thermal conductivities of platinum alloys at high temperatures, *Platinum Metals Rev* 49 (2005), 21–26.

8. G.W. Burns, M.G. Scroges, G.F. Strouse, M.L. Croarkin, and W.F. Guthrie, Temperature-electromotive force reference functions and tables for the letter designated thermocouple types based on the ITS-90, NIST Monograph 175 (1993).
9. Y.S. Touloukian and C.Y. Ho, Thermophysical properties of matter: The TPRC data series, Purdue University, Lafayette, IN, 1970.
10. A.J.C. Grellier, Characterisation of optical fibre tapering using a CO₂ laser, PhD. Thesis, Kent University, Canterbury, UK, 2000.
11. H. Scholze, Glass: Nature, structure and properties, Springer-Verlag, New York, 1991, p 208.
12. D. Tschumperlé and M. Nicolardot. Fiber cooling modelisation during draw using CFD, In: ASME CFD Symposium E13 (2001).
13. Flex PDE 2.13, PDE Solutions Inc (1999).
14. G. Rego, P.V.S. Marques, L.M.N.B.F. Santos, B. Schröder, J.L. Santos, and H.M. Salgado, Micro-sensor de temperatura isolado electricamente, PT 103160, (in Portuguese).

© 2008 Wiley Periodicals, Inc.

A NOVEL RING-WIDE BANDPASS FILTER BY USING ORTHOGONAL FEED STRUCTURE

Min-Hang Weng,¹ Shih-Kun Liu,² Yi-Ting Liu,² and Cheng-Yuan Hung³

¹ National Nano Device Laboratories, Taiwan

² Institute of Photonics and Communications, National Kaohsiung University of Applied Sciences, Kaohsiung, Taiwan

³ Department of Electronics Engineering and Computer Sciences, Tung-Fang Institute of Technology, Tung-Fang Taiwan;
Corresponding author: goliro.goliro@msa.hinet.net

Received 25 December 2007

ABSTRACT: In this article, a simple method to design a high-performance ring-wideband bandpass filter centered at 4 GHz without the perturbation element is presented. The coupling between the two orthogonal modes is accomplished by combining the resonant mode of the ring resonator and the resonant mode of the coupling line having a length about $\lambda g/4$ with respect to 4 GHz. This fabricated filter at center frequency f_0 of 4 GHz has showed very good measured characteristics, including a 3-dB fractional bandwidth of 40%, a very low insertion loss of 0.3 ± 0.1 dB, a stopband from 6 to 10 GHz, and a very high selectivity. © 2008 Wiley Periodicals, Inc. *Microwave Opt Technol Lett* 50: 2025–2027, 2008; Published online in Wiley InterScience (www.interscience.wiley.com). DOI 10.1002/mop.23577

Key words: ring resonator; wideband; bandpass; filter

1. INTRODUCTION

Microstrip ring resonator has been widely utilized to measure effective dielectric constant, dispersion, and discontinuity parameters of the dielectric layer [1–4]. Except the measurement applications, the microstrip ring resonator has also been used in filters, oscillators, mixers, and antennas [5] because of its advantages of compact size, easy fabrication, narrow passband bandwidth, and low radiation loss. The interesting compact filters such as dual-mode filters using microstrip ring resonators for cellular and other mobile communication systems have been reported [6]. The design of a planar dual-mode bandpass filter (BPF) was proposed by Wolff in the early 1970s [7]. The dual-mode BPF mainly consists of a physical coupling of two degenerate modes produced in a symmetrical ring or patch resonators excited by a perturbation element along the orthogonal plane of the resonator [8]. The dual-mode effects can be observed in the frequency responses, thus it is usually applied to design the narrow-band filter. Thus far, the

annular- and rectangular-ring resonators have been widely used for the design of dual-mode BPFs investigated by the transmission-line theory [9–12] and simulation tool [13]. However, the dual-mode ring or patch BPFs usually has narrow bandwidth due to their natural properties [1–3]. In 2003, Chang et al. first proposed a design of a planar dual-mode wideband BPF [4, 5], which used a ring resonator without the perturbation element and with direct-connected orthogonal feed lines and two tuning stubs to construct a wide passband with 3-dB fractional bandwidth ratio (FBW), defined as 3-dB bandwidth over designed center frequency) of 49.3%. However, the filter had serious spurious responses below or above the passband due to its direct-connected feed lines.

In this article, a ring-wide passband BPF without the perturbation element is presented. When the length of the coupling line is about $\lambda g/4$ with respect to 4 GHz, a FBW of 40% of the ring-wideband BPF can be obtained. A design technique using the IE3D electromagnetic (EM) simulator [14], which gives a full-wave solution via integral equations, and the method of moments (MoM) is presented in this article. Good agreement exists between the experimental results of the fabricated filter and the simulation results.

2. DESIGN OF RING WIDE BANDPASS FILTER

Figure 1 depicts the schematic of the proposed ring-wideband BPF (RW-BPF). The substrate used for simulation and fabrication in this study is the commercial substrate (RT/Duroid 5880) with dielectric constant (ϵ_r) of 2.2 and thickness (h) of 0.787 mm. The RW-BPF has a primary structure composed of square ring resonator and a pair of the coupling lines, as shown in Figure 1. The physical length L of the square ring resonator is designed to determine the fundamental center frequency. In the RW-BPF design, the coupling gap between the feed lines and the ring is selected for proper bandwidth.

In conventional dual-mode BPF design, the filter structure satisfies three conditions that (1) the input and output (I/O) ports connected to the center point of the coupling lines are separated orthogonally; (2) a perturbation element of generating a reflected wave against an incident wave is existed within the ring resonator; and (3) a symmetric plane is existed in the circuit geometry [2]. Unlike the conventional design, the proposed filter do not use a perturbation element and the two separated orthogonally I/O ports

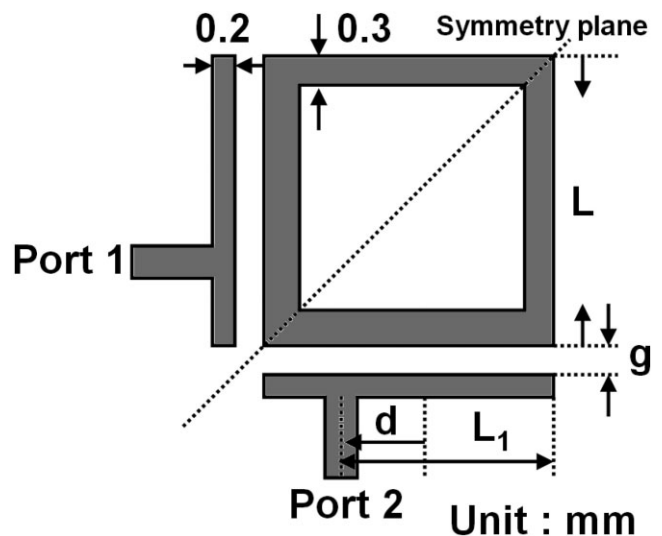


Figure 1 Practical layout of the designed RW-BPF designed on a 0.787-mm thick substrate with a dielectric constant of 2.2